Molecular recognition of two endogenous hormones by the human parathyroid hormone receptor-1

Li-Hua Zhao[1,2*]†, Qingning Yuan[1*], Antao Dai[1,3*], Chuan-Wei Chen[4], Xinheng He[1,2], Chao Zhang[5], Youwei Xu[1], Yan Zhou[1,3], Ming-Wei Wang[4,6,7], Dehua Yang[1,2,3]†, H. Eric Xu[1,2]†

[1]The CAS Key Laboratory of Receptor Research, Center for Structure and Function of Drug Targets, Shanghai Institute of Materia Medica, Chinese Academy of Sciences, Shanghai 201203, China

[2]University of Chinese Academy of Sciences, Beijing 100049, China

[3]The National Center for Drug Screening, Shanghai Institute of Materia Medica, Chinese Academy of Sciences, Shanghai 201203, China.

[4]Research Center for Deepsea Bioresources, Sanya, Hainan 572025, China.

[5]School of Pharmacy, Fudan University, Shanghai 201203, China.

[6]Department of Pharmacology, School of Basic Medical Sciences, Fudan University, Shanghai 200032, China

[7]Department of Chemistry, School of Science, The University of Tokyo, Tokyo 113-0033, Japan.

[*]These authors contributed equally: Li-Hua Zhao, Qingning Yuan and Antao Dai

†Correspondence: zhaolihuawendy@simm.ac.cn (Li-Hua Zhao); dhyang@simm.ac.cn (Dehua Yang); eric.xu@simm.ac.cn (H. Eric Xu)

ABSTRACT

Parathyroid hormone (PTH) and PTH-related peptide (PTHrP) are two endogenous hormones recognized by PTH receptor -1 (PTH1R), a member of class B G protein couple receptors (GPCRs). Both PTH and PTHrP analogs including teriparatide and abaloparatide, are approved drugs for osteoporosis, but they exhibit distinct pharmacology. Here we report two cryo-EM structures of human PTH1R bound to PTH and PTHrP in the G protein-bound state at resolutions of 2.6 and 3.2 Å, respectively. Detailed analysis of these structures uncovers both common and unique features for the agonism of PTH and PTHrP. Molecular dynamics (MD) simulation and together with site-directed mutagenesis studies reveal the molecular basis of endogenous hormones recognition specificity and selectivity to PTH1R. These results provide a rational template for the clinical use of PTH and PTHrP analogs as an anabolic therapy for osteoporosis and other disorders.

42 **INTRODUCTION**

43 Parathyroid hormone (PTH) and PTH-related protein (PTHrP) are two endogenous
44 peptide hormones that play key and distinct biological roles in skeletal development,
45 calcium- and phosphate- regulating actions, and bone turn over[1,2]. Lack of functional
46 PTH results in hypoparathyroidism[3], while overexpression of PTHrP derived from
47 tumor cells is the most common reason for cancer-associated hypercalcemia[4]. Both
48 PTH and PTHrP also have potent cardiovascular effects, including stimulating heart
49 rate increase independent of autonomic reflexes[5]. Both PTH and PTHrP exert their
50 effects on bone by activating the PTH type 1 receptor (PTH1R), primarily via G_s-cAMP
51 signaling[1,6]. High-resolution structures of PTH1R-G_s complexes bound to these
52 endogenous hormones are important for both pharmacological research as well as
53 clinical development aiming at PTH1R.

54

55 Osteoporosis is a disease of decreased bone mass, microarchitectural deterioration, and
56 fragility fractures. It is widespread and can affect all ethnic groups. Osteoporosis
57 becomes a major clinical problem in older women and men, especially in
58 postmenopausal women[7]. Clinical trials were proved that both PTH and PTHrP can
59 stimulate bone anabolism in patients with osteoporosis[6,8]. Teriparatide, recombinant
60 human parathyroid hormone encompassing residues 1-34 (PTH1-34), and
61 abaloparatide, recombinant human PTH-related protein encompassing residues 1-34
62 (PTHrP1-34), are two synthetic analogs of PTH and PTHrP. Although they exhibit
63 distinct pharmacology, they were the only two approved drugs by FDA for the treatment
64 of osteoporosis[6]. Recent studies suggest that PTH and PTHrP differ in their relative
65 capacities to bind to two pharmacologically distinguishable high-affinity PTH1R
66 conformations, R^0 (the G protein-uncoupled PTH1R conformation) and RG (the G
67 protein-coupled PTH1R conformation)[9,10]. PTH (1-34) can bind to the R^0 conformation
68 with the higher affinity than PTHrP (1-36) and prolonged cAMP responses[10]. Whereas
69 PTHrP (1-36) binds weakly to R^0, but it preferentially binds to the RG, promoted by
70 the over expression of a high affinity of $G\alpha_s$ and produce shorter cAMP responses[6,10].

Hattersley et al.[11] found that abaloparatide has similar high affinity to the RG as teriparatide, and abaloparatide shows more selectivity for the RG and a shorter cAMP signaling response compared to teriparatide. Abaloparatide and teriparatide different selectivity for the RG conformation can explain the different increase in bone mineral density (BMD) and different incidence of hypercalcemia in the clinical trials treated by abaloparatide and teriparatide[6]. Such conformational selectivity of receptor binding can be a key regulator of that ligand's biological activity, which provides an important clue to optimize conformational selective PTH and PTHrP analogs for a new treatment option for PTH-related disorders[12].

Up to now, the most effective treatments of osteoporosis are based on daily injections teriparatide or abaloparatide. These therapies are both costly and inconvenient in clinical application due to the therapy by injection. However, there are no available small-molecule agonist drugs for the treatment of osteoporosis, in part due to lack of detailed structure information of an intact endogenous peptide-PTH1R-G-protein complex[13,14]. The only available structure of the full-length PTH1R is in complex with a synthetic long-acting PTH (LA-PTH), which reveals extensive interactions of LA-PTH with PTH1R[2]. The detailed structural and mechanistic understanding of the receptor activation by endogenous peptide hormones is critical for explaining how PTH and PTHrP mediate their distinct biologic actions via a common receptor and for aiding the rational development of new drug therapies targeting PTH1R. Therefore, we determined two cryo-electron microscopy (cryo-EM) structures of the active PTH1R–G_s complexes bound to PTH and PTHrP to provide insights into the pharmacological mechanisms for the clinical use of endogenous and clinical ligands.

Materials and Methods

Constructs

The human PTH1R (residues 27-502) with G188A and K484R mutations was cloned into pFastBac vector (Invitrogen) with the haemagglutinin signal peptide (HA)

100 followed by a TEV protease cleavage site and a double MBP (2MBP) tag to facilitate
101 expression and purification[2]. To facilitate a stable complex, the above PTH1R construct
102 was added the LgBiT subunit (Promega) at the C terminus of PTH1R. A bovine
103 dominant-negative human $G\alpha_s$ ($DNG\alpha_s$) with mutations G226A and A366S, is a
104 chimera that the AHD of $G\alpha_s$ (69-205) was replaced with $G\alpha_i$ (62-182) to bind to the
105 Fab_G50[2]. Based on the published $DNG\alpha_s$, a modified bovine $G\alpha_s$ ($mDNG\alpha_s$), its N
106 terminus (M1–K25) and α-helical domain (AHD, F68–L203) of $G\alpha_s$ were replaced by
107 the N terminus (M1–M18) and AHD (Y61–K180) of the human $G\alpha_i$, which can bind
108 scFv16 and Fab_G50[18] and the residues N254-T263 of $G\alpha_s$ were deleted. In addition,
109 eight mutations (G49D, E50N, L63Y, A249D, S252D, L272D, I372A, and V375I). To
110 facilitate the folding of the G protein, $DNG\alpha_s$ and $mDNG\alpha_s$ was co-expressed with
111 GST-Ric-8B[19]. Rat Gβ1 with an N-terminal
112 MHHHHHHSSGLVPRGSHMASHHHHHHHHHH-tag (His16) was fused with the
113 SmBiT subunit (peptide 86, Promega)[20] via a 15 amino acid (GSSGGGGSGGGGSSG)
114 linker at its C terminus. In addition, to clone the constructs into the pcDNA3.1 vector
115 (Promega) for cAMP accumulation, all constructs were cloned using homologous
116 recombination (Clone Express One Step Cloning Kit, Vazyme).
117
118 Protein expression
119 The PTH1R and G proteins were co-expressed in *Sf9* insect cells (Invitrogen). When
120 the cells grew to a density of 3.5×10^6 cells/mL in ESF 921 cell culture medium
121 (Expression Systems), we infected the cells with five separate virus preparations at a
122 ratio of 1:2:2:2:2 for PTH1R(27-502)-LgBiT-2MBP, $DNG\alpha_s$ or $mDNG\alpha_s$, His16-Gβ1-
123 peptide 86, Gγ2, and GST-Ric-8B. The infected cells were cultured at 27°C for 48 h
124 before collection by centrifugation and the cell pellets were stored at −80°C.
125
126 Expression and purification of Nb35
127 Nanobody-35 (Nb35) was expressed in *E. coli* BL21 cells, the cultured cells were
128 grown in 2TB media with 100 μg/mL ampicillin, 2 mM $MgCl_2$, 0.1% glucose at 37°C

129 for 2.5 h until OD600 of 0.7-1.2 was reached. Then the culture was induced with 1 mM
130 IPTG at 37°C for 4-5 h, and harvested and frozen at -80°C until use. Nb35 was purified
131 by nickel affinity chromatography and followed by size-exclusion chromatography
132 using HiLoad 16/600 Superdex 75 column following overnight dialysis against 20 mM
133 HEPES, pH 7.4, 100 mM NaCl, 10% glycerol. The quality of purified protein was
134 verified by SDS-PAGE and store at -80 °C.
135
136 Complex purification
137 The complexes were purified according to previously described methods[21,22]. It was
138 resuspended in 20 mM HEPES pH 7.4, 100 mM NaCl, 10 mM $MgCl_2$, 10 mM $CaCl_2$,
139 2 mM $MnCl_2$, 10% glycerol, 0.1 mM TCEP, 15 μg/mL Nanobody (Nb35), 25 mU/mL
140 apyrase (Sigma), 12 μM PTH1-34 (Synpeptide Co., Ltd) and 12 μM PTHrP1-36
141 (TGpeptide Biotechnology Co., Ltd), supplemented with Protease Inhibitor Cocktail
142 (TargetMol, 1 mL/100 mL suspension). The lysate was incubated for 1 h at room
143 temperature and complex from membranes solubilized by 0.5% (w/v) lauryl maltose
144 neopentylglycol (LMNG, Anatrace) supplemented with 0.1% (w/v) cholesteryl
145 hemisuccinate TRIS salt (CHS, Anatrace) for 2 h at 4°C. The supernatant was isolated
146 by centrifugation at 65,000 × g for 40 min, and the solubilized complex was incubated
147 with Amylose resin (NEB) for 2 h at 4°C. The resin was loaded onto a plastic gravity
148 flow column and washed with 15 column volumes of 20 mM HEPES, pH 7.4, 100 mM
149 NaCl,10% glycerol,10 mM $MgCl_2$, 1 mM $MnCl_2$, 0.01% (w/v) LMNG, 0.01% glyco-
150 diosgenin (GDN, Anatrace) and 0.004% (w/v) CHS, 2 μM PTH1-34 or 2 μM PTHrP1-
151 36, and 25 μM TCEP. After washing, the protein was treated overnight with TEV
152 protease on column at 4°C. Next day the flow through was collected and concentrated,
153 then UCN1-CRF2R-G_o and UCN1-CRF2R-G_{11} were loaded onto a Superdex200
154 10/300 GL column and Superose6 Increase 10/300GL (GE Healthcare), respectively,
155 with the buffer containing 20 mM HEPES, pH 7.4, 100 mM NaCl, 2 mM $MgCl_2$,
156 0.00075% (w/v) LMNG, 0.00025% GDN, 0.0002% (w/v) CHS, 2 μM PTH1-34 or 2
157 μM PTHrP1-36, and 100 μM TCEP. The complex fractions were collected and

concentrated individually for electron microscopy experiments.

Cryo-EM data acquisition

For the preparation of cryo-EM grids, 2.5 μL of the purified PTH-PTH1R-G_s and PTHrP-PTH1R-G_s complexes at a concentration of ~8.4 mg/mL and ~5.1 mg/mL were respectively applied to the glow-discharged Au 300 mesh holey carbon grids (Quantifoil R1.2/1.3). The grids were blotted and then plunge-frozen in liquid ethane using a Vitrobot Mark IV (ThermoFisher Scientific) at 4°C.

Cryo-EM images of PTH-PTH1R-G_s were collected on a Titan Krios G4 equipped with a Gatan K3 direct electron detector with super-resolution mode and EPU were used to acquire cryo-EM movies at Advanced Center for Electron Microscopy at Shanghai Institute of Materia Medica, Chinese Academy of Sciences. A total of 8,002 Movies were recorded with pixel size of 0.824 Å at a dose of 50 electron per $Å^2$ for 36 frames. The defocus range of this dataset was -0.8 μm to -1.8 μm. For dimer complex, another 5,054 movies ware obtained with same parameters.

Cryo-EM images of the PTHrP-PTH1R-G_s complex were collected on a Titan Krios G4 at 300KV accelerating voltage equipped with Gatan K3 direct electron detector. A total of 7,266 movies were recorded with pixel size of 0.824 Å at a dose of 50 electron per $Å^2$ for 36 frames. The defocus range of this dataset was -0.8 μm to -1.8 μm.

Image processing

All dose-fractionated image stacks were subjected to beam-induced motion correction by RELION-4.0[23]. The defocus parameters were estimated by CTFFIND 4.1[24]. PTH-PTH1R-G_s complex and dimer complex, by auto-picking yielded 3,051,218 particles and 10,497,057 which were processed by reference-free 2D classification using Cryosparc[25]. With initial model, after several rounds of 3D classification using RELION, 407,467 particles and 55,858 particles were used to further refinement and

187 polishing, yielding two reconstructions with global resolution of 2.62 Å and 3.72 Å
188 respectively, and subsequently post-processed by DeepEMhancer[26].
189
190 For the PTHrP-PTH1R-G_s complex, movies were aligned with RELION-4.0[23]. Initial
191 contrast transfer function (CTF) fitting was performed with CTFFIND4.1[24] from
192 Cryosparc[25]. Auto-picking and two-dimensional (2D) Classification were processed
193 using Cryosparc, producing 7,700,728 particles for further processing. With initial
194 model, two rounds of 3D classifications were carried out. A further one round of 3D
195 classification was conducted with a mask on the receptor, in which 436,359 particles
196 were subjected to 3D auto-refinement and polishing. A map with an indicated global
197 resolution of 3.25 Å at a Fourier shell correlation (FSC) of 0.143 was generated from
198 the final 3D refinement, and subsequently post-processed by DeepEMhancer[26].
199
200 Model building and refinement
201 The cryo-EM structure of the LA-PTH1R-G_s-Nb35 complex (PDB code 6NBF) and
202 two ECD crystal structures (PDB: 3C4M and PDB: 3H3G) were used as the start for
203 model building and refinement against the electron microscopy map. The model was
204 docked into the electron microscopy density map using Chimera[27], followed by iterative
205 manual adjustment and rebuilding in COOT[28]. Real space and Rosetta refinements were
206 performed using Phenix[29]. The model statistics were validated using MolProbity[30].
207 Fitting of the refined model to the final map was analyzed using model-versus-map
208 FSC. To monitor the potential over-fitting in model building, FSC_{work} and FSC_{free} were
209 determined by refining 'shaken' models against unfiltered half-map-1 and calculating
210 the FSC of the refined models against unfiltered half-map-1 and half-map-2. The final
211 refinement statistics are provided in Supplementary Table 2. Structural figures were
212 prepared in Chimera and PyMOL (https://pymol.org/2/).
213
214 Molecular dynamics simulations
215 The cryo-EM structures of PTH34-PTH1R-G_s complex and PTHrP-PTH1R-G_s

complex were used for the construction of MD simulation systems. Missing ICL3 and short part before TM1 were supplied according to the loop builder program in Molecular Operation Environment. Missing N-terminal and ECL1 structures were constructed according to the AlphaFold2 models[31]. The mutation G188A was modified back and the G proteins were removed. Using CHARMM-GUI, the models were inserted in POPC (palmitoyl-2-oleoyl-sn-glycerol-3-phosphocholine) lipids[32,33]. The length of X and Y were both 130 Å. TIP3P waters and 0.15 M NaCl under a periodic boundary condition were also added to systems. The force fields for proteins and lipids were FF19SB and lipid17, respectively[34-36]. We used hydrogen mass repartitioning during system construction.

After preparation, the systems first encountered a minimization process of 5,000 steepest descent cycles with a constraint on backbone atom, sidechain atom, and lipid coordinates. Then, the constraints were generally decreased in the separated 6 steps of the equilibration process provided by CHARMM-GUI. The first three of them had a timestep of 1 fs and heated the system to 303.15 K, 1 atm in 375 ps. The last three of them had 2 fs timestep and decreased constrain in the coming 1.5 ns. We then performed the independent 400 ns × 6 MD simulations on Amber 20. During simulations, the Langevin thermostat and Berendsen barostat were used for temperature (300 K) and pressure (1 atm) control. Long-range electrostatic interactions were treated by the Particle mesh Ewald and a 10 Å cutoff was employed for short-range interactions. In the following analysis, tICA was calculated in MSMbuilder[37] and the representative structures were extracted by CPPTRAJ[38]. MMGBSA were calculated by Maestro, Schrödinger.

cAMP accumulation assay

PTH and PTHrP stimulated cAMP accumulation was measured by a LANCE Ultra cAMP kit (PerkinElmer). After 24 h culture, the transfected cells were seeded into 384-well microtiter plates at a density of 3,000 cells per well in HBSS supplemented with

245 5 mM HEPES, 0.1% (w/v) BSA or 0.1% (w/v) casein and 0.5 mM 3-isobutyl-1-
246 methylxanthine. The cells were stimulated with different concentrations of peptide
247 agonists for 40 min at RT. Eu-cAMP tracer and ULight^{TM}-anti-cAMP were then diluted
248 by cAMP detection buffer and added to the plates separately to terminate the reaction.
249 Plates were incubated at RT for 1 h and the fluorescence intensity measured at 620 nm
250 and 665 nm by an EnVision multilabel plate reader (PerkinElmer).
251
252 Statistical analysis
253 All functional data were displayed as means ± standard error of the mean (S.E.M.).
254 Statistical analysis was performed using GraphPad Prism 8.0 (GraphPad Software).
255 Experimental data were evaluated with a three-parameter logistic equation. The
256 significance was determined with either two-tailed Student's t-test or one-way ANOVA.
257 $P < 0.05$ was considered statistically significant.
258
259 Data availability
260 Cryo-EM maps have been deposited in the Electron Microscopy Data Bank under
261 accession codes: EMD-XXX (PTH-bound PTH1R-G_s complex), EMD- XXX (PTH-
262 bound PTH1R-G_s complex). The atomic coordinates have been deposited in the Protein
263 Data Bank under accession codes: XXX (PTH-bound PTH1R receptor) and XXX
264 (PTHrP-bound PTH1R receptor).
265
266 **RESULTS**
267 Structural determination
268 Stable PTH1R-G_s protein complex can be assembled with LA-PTH, but not with PTH
269 and PTHrP. To overcome this technical obstacle, we employed the NanoBiT tethering
270 strategy to stabilize the PTH1R-G_s protein complex assembly with PTH and PTHrP
271 (Supplement Fig.1). The PTH1R was co-expressed with $G\alpha_s$, Gβ1, Gγ2 and GST-Ric-
272 8B. Nanobody 35 (Nb35) was added into membranes to stabilizing the receptor-G
273 protein complex according to the method previously described[2] (Supplement Fig. 1).

The complex structures of the G_s-coupled PTH1R bound to PTH and PTHrP were determined by cryo-EM to the resolutions of 2.6 Å and 3.2 Å, respectively (Fig. 1 and Supplementary Fig. 2-3, Supplementary Table 1). In addition, we applied extensive particle classifications that yielded a distinct subclass of a dimeric form of the PTH-PTH1R-G_s complexes, which was determined to a resolution of 3.7 Å (Supplementary Fig. 4). Because this dimeric form is mediated through no-physiological Nb35 and G_s interface, no further discussion is presented in the paper. Both endogenous peptide-PTH1R-G_s complexes are similar to other GPCR-G protein complex structures, the α-helical domain (AHD) of G_s is flexible and invisible. Apart from extracellular domain (ECD) of receptor, the majority of the amino acid side chains of receptor and heterotrimeric G_s protein were well resolved in the final models, which are refined against the EM density map with excellent geometry. Both peptides, PTH (1-34) and PTHrP (1-36) were clearly identified, thus providing reliable models for the mechanistic explanation of pharmacological actions of teriparatide and abaloparatide at PTH1R (Supplement Fig. 5). In addition, like LA-PTH-PTH1R-G_s complex, an ordered annular lipid band wrapping around the periphery of the receptor transmembrane domain (TMD) is visible in the cryo-EM map, among which several lipid molecules were built (Fig. 1a-e). These structural lipids possibly stabilize the PTH1R in its active state.

Overall structures of G_s-coupled PTH1R bound to PTH and PTHrP

Both PTH-PTH1R-G_s and PTHrP-PTH1R-G_s complex structures closely resemble that of the LA-PTH-PTH1R-G_s complex with the root mean square deviation (RMSD) value of 0.5 Å for whole complexes, 0.7 Å for G_s alone, 0.5 Å for receptor alone (Fig. 2). Notable conformational differences were observed in the position and orientation of the C-terminal fragment of peptide and the ECD of receptor. The C-terminal fragment of PTH and PTHrP in complexes are shifted away TM7 by ~9.6 Å and 2.6 Å (measured at Cα of H^{32P}), respectively, relative to their positions in the LA-PTH-bound structure

303 (PDB: 6NBF) [2]. The receptor ECD-α1 helix in the PTH- and PTHrP-bound structures
304 are shifted away TM7 by ~10 Å and 7.1 Å (measured at Cα of $K50^{ECD}$), respectively,
305 relative to their positions in the LA-PTH-bound structure (Fig. 2a-c). These
306 conformational changes allow the C-terminal fragment of hormone bind specificity to
307 PTH1R, indicating PTH1R-associated peptide recognition specificity. Except ECD-α1
308 helix in PTH-PTH1R cryo-EM structure is shifted away PTH by ~2 Å, relative to X-
309 ray structure (measured at Cα of $K50^{ECD}$), the overall conformation of the PTH-receptor
310 ECD and PTHrP-receptor ECD in PTH-PTH1R cryo-EM structures resemble the
311 previously published crystal structures of PTH-ECD and PTHrP-ECD complexes (PDB:
312 3C4M and 3H3G) [9,15], respectively. The structural basis for the binding specificity of
313 PTH and PTHrP to PTH1R is relatively consistent with the crystal structures (Fig. 2d).
314
315 Molecular basis for recognition of PTH and PTHrP by PTH1R
316 Both PTH-PTH1R-G_s and PTHrP-PTH1R-G_s complexes exhibit a similar and unique
317 peptide-receptor binding interface, which is consistent with the "two-domain" model
318 of the peptide-PTH1R interaction mechanism of hormone recognition common to class
319 B GPCRs (Fig. 3). In these complexes, PTH and PTHrP adopt an amphipathic helix
320 with their N terminus dipping into the receptor TMD, while the C terminus is closely
321 interaction with the ECD. The N-terminal fragment of PTH (residues 1-14, PTH^N) and
322 PTHrP (residues 1-15, $PTHrP^N$) bind to the TMD and activate the receptor. The PTH^N
323 and $PTHrP^N$ adopt four helical turns and insert deeply into the TMD pocket. PTH^N and
324 $PTHrP^N$ are directly surrounded by TM1, TM2, TM3, TM5, TM6 and TM7 and form
325 extensive interactions with the TMD core. PTH^N and $PTHrP^N$ can also interact with
326 ECL2 and ECL3 of receptor. The C-terminal fragment of PTH (residues 15-34, PTH^C)
327 and PTHrP (residues 16-34 $PTHrP^C$) bind to the ECD of PTH1R to confer high affinity
328 and specificity to the receptor (Fig. 3a, d).
329
330 In line with a similar conformation observed between the cryo-EM structures and
331 crystal structures of the PTH1R ECD bound PTH and PTHrP, the extensive interactions

332 of the ECD with PTH^{C} and $PTHrP^{C}$ in cryo-EM structure complexes are similar to those
333 observed in the previously reported X-ray structures of peptide-ECD complexes (Fig.
334 3b, e). In the PTH-PTH1R-G_s complex, the hydrophobic residues V21, W23, L24, L28,
335 V31 and F34 of the PTH, form an extensive hydrophobic interactions with the
336 hydrophobic groove of the three-layer PTH1R-ECD fold (Fig. 3b)[15]. In the PTHrP-
337 PTH1R-G_s complex, the conserved ECD fold also shows the hydrophobic contacted
338 with F23, L24, L27, I28, I31 and I36 of PTHrP (Fig. 3e)[9]. In addition, $N16^{PTH}$ and
339 $Q16^{PTHrP}$ form a hydrogen bond with $E35^{ECD}$ and $T33^{ECD}$, respectively. The conserved
340 amino acid R20 in the PTH and PTH-related ligands also forms a hydrogen bond with
341 the backbone carbonyls of $M32^{ECD}$ of PTH1R and forms electrostatic interactions with
342 $D137^{ECD}$. These polar interactions display the binding affinity and specificity of PTH
343 and PTHrP to PTH1R. This amino acid R20 is conserved in all three endogenous
344 peptide hormones of PTH1R and PTH2R but distinct from other class B GPCRs,
345 suggesting that R20 is critical for peptide hormones recognition and specificity of PTH
346 and PTH-related ligands[15]. Except for these conserved interaction, these two peptide
347 hormones also interact with PTH1R in a peptide-specific mode. $E19^{PTH}$ forms
348 electrostatic interaction with $K34^{ECD}$, $V21^{PTH}$ makes hydrophobic contact with
349 $D137^{ECD}$ and $W23^{PTH}$ makes Pi interaction with $K34^{ECD}$ and hydrophobic interaction
350 with $Q37^{ECD}$ and $I38^{ECD}$. But different amino acids at cognate positions of PTHrP,
351 $R19^{PTHrP}$ and $R21^{PTHrP}$ form electrostatic interaction with $E35^{ECD}$, $D137^{ECD}$,
352 respectively and $F23^{PTHrP}$ makes hydrophobic interaction with $I38^{ECD}$ and $L41^{ECD}$ of
353 PTH1R (Fig. 3b, e). These interactions receive support from our mutagenesis studies
354 by measuring cAMP responses. Alanine substitution of $D137^{ECD}$ and $Y167^{ECD}$ of
355 PTH1R shows clearly a great reduction in the potency of both PTH and PTHrP-
356 mediated G_s activation (Fig. 3g-h, Supplementary Table 2). In additional, both alanine
357 substitution $M32^{ECD}$ and $E35^{ECD}$ also diminish the potency of PTHrP and slightly
358 decreased the efficacy of PTH. These amino acid residues are important for determining
359 the affinity and specificity of PTH and PTHrP to PTH1R.
360

361 The sequences of PTH^N, $PTHrP^N$ and other PTH-related ligands highly resemble.
362 Although $PTHrP^N$ can overlapped well with LA-PTH^N, while PTH^N is different from
363 their positions. Every one of the three N-terminal peptide helix inserts into the receptor
364 TMD core by a analogical angle and orientation, thereby revealing a similar peptide
365 hormones recognition and activation mechanism (Fig. 2c, f and supplementary Fig. 6).
366 Both PTH^N and $PTHrP^N$ run parallel to TM2, making extensive contacts with the
367 residues in TM1, TM2, TM3, TM5, TM6, TM7 and ECL2 and ECL3 (Fig. 3c, f).
368 Especially the first six residues of PTH^N and $PTHrP^N$ play critical roles in the receptor
369 activation. In contrast, PTH (7-34) and PTHrP (7-34) are potent antagonists of PTH
370 receptor[1]. For PTH, A1 forms a hydrogen bond with $T427^{6.59b}$ and makes hydrophobic
371 contacts with $Q364^{5.40b}$, $M425^{6.57b}$ and $Q440^{7.38b}$. For PTHrP, S1 makes more polar
372 interactions with $F424^{6.56b}$, $M425^{6.57b}$, $T427^{6.59b}$ and $Q440^{7.38b}$. These observations
373 provide support for our mutagenesis studies by measuring cAMP responses. Alanine
374 substitutions of $Q364^{5.40b}$, $M425^{6.57b}$ and $Q440^{7.38b}$ notably reduce the potency PTHrP-
375 mediated G_s activation, and slightly effect on the potency of PTH in G_s activation. (Fig.
376 3i-g, Supplementary Table 2). The same amino acid V2 in two peptides makes extensive
377 hydrophobic contacts with $L292^{3.40b}$, $Q364^{5.40b}$ and $I367^{5.43b}$. Mutation of $L292^{3.40b}$
378 remarkably reduce pEC_{50} and E_{max} values in the PTH- and PTHrP-induced receptor
379 activity (Fig. 3i-g, Supplementary Table 2). Although S3 in the same position, they
380 exhibit different binding interaction with receptor. $S3^{PTH}$ makes hydrophobic contacts
381 with $Q440^{7.38b}$, $M441^{7.39b}$ and $M445^{7.43b}$. While $S3^{PTHrP}$ forms polar interactions with
382 $E444^{7.42b}$, $N448^{7.46b}$, and also makes hydrophobic interaction with $M445^{7.43b}$. alanine
383 substitutions of $M445^{7.43b}$ indicates a great reduction in the potency of PTHrP-mediated
384 G_s activation (Fig. 3j, Supplementary Table 2), but almost no effect on the receptor
385 activity by PTH in G_s activation (Fig. 3i, Supplementary Table 2). E4 in both PTH and
386 PTHrP, forms the stabilizing hydrogen bond interact and salt bridge with $Y195^{1.47b}$ and
387 $R233^{2.60b}$, respectively. Both alanine mutations in $Y195^{1.47b}$ and $R233^{2.60b}$ remarkably
388 reduce peptide-mediated PTH1R activation, indicating that E4 of the peptide is a key
389 role for peptide-induced receptor activation (Fig. 3i-j, Supplementary Table 2). $I5^{PTH}$

390 makes hydrophobic contacts with L289$^{3.37b}$, L292$^{3.40b}$ and Q364$^{5.40b}$. While H5^{PTHrP} at
391 the same position of PTHrP not only makes extensive hydrophobic interactions with
392 L289$^{3.37b}$, K360$^{5.36b}$ and I363$^{5.39b}$, but also forms an additional electrostatic interaction
393 with Q364$^{5.40b}$. Q6 of PTH and PTHrP forms highly conserved hydrophobic interactions
394 with Y429^{ECL3}, W437$^{7.35b}$, Q440$^{7.38b}$ and M441$^{7.39b}$. All of these residues mutations,
395 Y429^{ECL3}A, W437$^{7.35b}$A, Q440$^{7.38b}$A and M441$^{7.39b}$A reduce both PTH and PTHrP to
396 activate PTH1R. In additional, N10^{PTH} is hydrogen-bonded with W437$^{7.35b}$, the same to
397 PTH position, D10^{PTHrP} also forms a hydrogen-bond with W437$^{7.35b}$. W437$^{7.35b}$A,
398 markedly reduce both PTH and PTHrP to activate PTH1R, supporting the fact that
399 N10^{PTH} and D10^{PTHrP} of the peptide are critical for two endogenous hormones-induced
400 receptor activation (Fig. 3i-j, Supplementary Table 2). H9 in both PTH and PTHrP
401 interacts with ECL2 and ECL3 of receptor, such as the hydrophobic interactions with
402 D353^{ECL2}, S355^{ECL2}, and electrostatic interaction with Y429^{ECL2}. D353^{ECL2}
403 significantly decreases the PTHrP-induced PTH1R activation (Fig. 3j, Supplementary
404 Table 2), but almost no effect on the receptor activity by PTH in G_s activation (Fig. 3i,
405 Supplementary Table 2). In additional, L7$^{PTH/PTHrP}$, M8^{PTH} or L8^{PTHrP}, L11^{PTH} or
406 K11^{PTHrP}, G12$^{PTH/PTHrP}$, K13$^{PTH/PTHrP}$, H14^{PTH} or K14^{PTHrP} can form extensive
407 hydrophobic interactions with the TMD core and ECL2. The above interactions of
408 peptide^{N} with the TMD provide the major binding and activation energy for the
409 formation of the signal complex. Therefore, the stability of the interface between
410 peptide^{N} and the TMD is well supported by an extensive network of complementary
411 polar and non-polar interactions between the bound PTH and PTH-related ligands and
412 the TMD. The detailed interactions listed in Fig. 2c, f and supplementary Fig. 6. These
413 interactions help to explain the rich and distinct pharmacology of PTH and PTHrP
414 acting through the same receptor.
415
416 Activation mechanism of PTH1R
417 Comparison of the PTH- and PTHrP-bound PTH1R-G_s complex structures with LA-
418 PTH-bound PTH1R-G_s complex structure reveals a remarkably similarity in the G

419 protein binding interface, indicating a common mechanism for G protein coupling
420 specificity (Fig. 4). $G\alpha_s$-α5 helix dipped into the cytoplasmic receptor cavity and forms
421 important interactions with TM2, TM3, TM5, TM6, H8 and intracellular loop 3(ICL3)
422 (Fig. 4c-d). In all three PTH1R-G_s complex structures, L393 in $G\alpha_s$-α5 helix make polar
423 interaction with S409$^{6.41b}$. Both D381 and Q384 of $G\alpha_s$-α5 helix form an electrostatic
424 interaction with K388$^{5.64b}$. R385 of $G\alpha_s$-α5 also makes an additional electrostatic
425 interaction with E391^{ICL3} of PTH1R in PTH-bound PTH1R-G_s complex and PTHrP-
426 bound PTH1R-G_s complex. E392 forms polar interaction with the backbone amine of
427 N363$^{8.47b}$ and G364$^{8.48b}$. The bulky residue Y391 at the $G\alpha_s$-α5 helix C terminus binds
428 to a sub-pocket formed by R219$^{2.46b}$, H233$^{2.50b}$, Y305$^{3.53b}$ and L306$^{3.54b}$ in PTH1R. The
429 hydrophobic residues L388, Y391, L393 and L394 of $G\alpha_s$-α5 helix form extensive
430 hydrophobic interaction with TMD helixes (Fig. 4c-d). F314^{ICL2} in PTH- and PTHrP-
431 bound PTH1R-G_s complexes insert into a cavity formed by αN-β1 junction and α5 of
432 $G\alpha_s$ and make hydrophobic interactions for stabilizing the interface, but they are
433 different from LA-PTH-bound PTH1R-G_s complex, which F314^{ICL2} not directly
434 interact with the hinge region of the $G\alpha_s$ protein (Fig. 4e). Both in PTH- and PTHrP-
435 bound PTH1R-G_s complex, the electrostatic interactions presented between R214^{ICL1}
436 and D312 of Gβ1, and in PTH- and LA-PTH- bound PTH1R-G_s complex, hydrogen
437 bonds between R476$^{8.60b}$ and the backbone oxygen of G310 of Gβ1, while in PTHrP-
438 bound PTH1R-G_s complex, hydrogen bonds between R472$^{8.56b}$ and the backbone
439 oxygen of G310 of Gβ1. Additional contacts between R213^{ICL1} and R52 of Gβ1 in PTH-
440 bound PTH1R-G_s complex and in LA-PTH-bound PTH1R-G_s complex, all of these
441 interactions may stabilize the interface of helix 8 and Gβ1 (Fig. 4f).
442
443 Conformational changes during PTH1R activation
444 PTH1R has two different conformation states, the G-protein free state R^0 and the G
445 protein coupled state RG[10]. During peptide-bound PTH1R activation, two PTH1R
446 conformations undergo different rearrangement of the network residues to facilitate the
447 ligand binding and signal transduction[14]. Based on structural alignment of PTH1R:

448 agonist complex in the absence of G protein, with three G protein-bound PTH1R (RG):
449 agonist complexes shows different conformational changes, involving the ECD and the
450 TMD of the receptor (Fig. 5a-c). The receptor ECD-α1 in the PTH-bound and PTHrP
451 bound PTH1R RG structures are shifted away TM7 by ~4.4 Å and 3.5 Å (measured at
452 Cα of $K50^{ECD}$), respectively, relative to their positions in the ePTH-bound PTH1R
453 structure. The main conformational changes happens in TMD (Fig. 5b-c). The class B
454 GPCRs conserved PxxG motif ($P415^{6.48b}$, $L416^{6.48b}$, $F417^{6.49b}$ and $G418^{6.50b}$) in three
455 agonist-G-protein-bound PTH1R complexes caused a notable conformational
456 rearrangement and make TM6 kink outward ~90° in the middle (Fig. 5d). The TM6
457 sharp kink creating an intracellular binding pocket for the C terminus of Gα, thereby
458 enabling intracellular G protein activation and signal transduction. Meanwhile, the kink
459 of TM6 together with other conformational changes caused three class B GPCRs
460 conserved polar interaction networks rearrangement, including HETY network
461 ($H223^{2.50b}$, $E302^{3.50b}$, $T410^{6.42b}$, and $Y457^{7.57b}$), the II-VI-VII-VIII network ($R219^{2.46b}$,
462 $K405^{6.37b}$, $N463^{7.61b}$ and $E465^{8.49b}$) and central polar network ($R233^{2.60b}$, $N295^{3.43b}$,
463 $H420^{6.52b}$ and $Q451^{7.49b}$). However, this structural hallmark of class B GPCRs activation
464 was not observed in the ePTH-PTH1R complex structure and CLR-CGRPR-RAMP1
465 complex structure, which are in the absence of G protein. Their intracellular part of the
466 receptors still displays the hallmarks of an inactive conformation (Fig. 5b and
467 supplementary Fig. 7), which are called intermediate states on the transition of the
468 receptor toward the G protein-bound state[13,14,16]. The intermediate states of class B
469 GPCRs and the R^0 conformation of the PTH1R resemble in agonist binding and in the
470 absence of G protein. The ability of PTH and PTHrP to bind to RG is similar, but PTH
471 has a greater capacity to bind to R^0 state[1,10]. Such conformational selectivity mediate
472 their distinct biological actions[10]. From molecular dynamics (MD) simulations, the
473 lower R^0 binding ability of PTHrP was attributed to its higher binding free energy upon
474 specific states (Supplementary Fig. 8). Although the capacity of PTH and PTHrP to
475 bind to R^0 is different, these peptides can bind to the G protein-coupled PTH1R
476 complex (RG) with a highly similar G protein binding interface, suggesting a common

mechanism for G_s engagement.

DISCUSSION

The cryo-EM structures of PTH-PTH1R-G_s and PTHrP-PTH1R-G_s complexes further reveal the structural basis for recognition of PTH and PTHrP by PTH1R and the receptor activation and G protein-coupling mechanisms, providing an opportunity to use these structures as modules for designing new PTH replacement therapies in the future. Two synthetic analogs of PTH and PTHrP, teriparatide and abaloparatide were approved drugs by FDA and used in clinic, but as conventional therapy for osteoporosis by daily injections with high costs, probably not suitable for treating such a widespread disease. Therefore, PTH1R-specific targeted orally agonists for osteoporosis are urgently developed. To our knowledge, PTH and PTHrP differ in selectivity for two pharmacologically distinguishable high-affinity PTH1R conformations, R^0 and RG^1. Such R^0-selective analogs, including PTH, M-PTH (1-28) and M-PTH (1-34) display high affinity binding to R^0 as well as notably mediate prolonged cAMP signaling responses and are now being investigated as potential new drugs for treating hypoparathyroidism[17]. While another PTH analogs, such as PTHrP (1-36) and M-PTH (1-14) exhibit a high- affinity to bind to RG conformation, and produces a shorter-lived and more pulsatile action at the receptor, might prove to be more efficacious in this class of patients[1,12]. Mutational studies of the ligand-receptor binding sites indicate that the binding specificity of PTH and PTHrP to PTH1R. According to our structures, detailed patterns of teriparatide and abaloparatide-receptor interactions can be identified and it can explain the binding specificity of PTH and PTHrP to PTH1R. Thus, a detailed understanding of PTH and PTHrP binding and activation of PTH1R provide a rational template to development of optimized therapeutics targeting PTH1R diseases.

REFERENCES

1 Gardella, T. J. & Vilardaga, J. P. International Union of Basic and Clinical Pharmacology. XCIII. The parathyroid hormone receptors--family B G protein-coupled receptors. *Pharmacol Rev* **67**, 310-337, doi:10.1124/pr.114.009464 (2015).

2 Zhao, L. H. *et al.* Structure and dynamics of the active human parathyroid hormone

receptor-1. *Science* **364**, 148-153, doi:10.1126/science.aav7942 (2019).

3 Nishimura, Y. *et al.* Lead Optimization and Avoidance of Reactive Metabolite Leading to PCO371, a Potent, Selective, and Orally Available Human Parathyroid Hormone Receptor 1 (hPTHR1) Agonist. *J Med Chem* **63**, 5089-5099, doi:10.1021/acs.jmedchem.9b01743 (2020).

4 Kir, S. *et al.* Tumour-derived PTH-related protein triggers adipose tissue browning and cancer cachexia. *Nature* **513**, 100-104, doi:10.1038/nature13528 (2014).

5 Wider, J., Undyala, V. V. R., Lanske, B., Datta, N. S. & Przyklenk, K. Parathyroid Hormone-Related Peptide and Its Analog, Abaloparatide, Attenuate Lethal Myocardial Ischemia-Reperfusion Injury. *J Clin Med* **11**, doi:10.3390/jcm11092273 (2022).

6 Chew, C. K. & Clarke, B. L. Abaloparatide: Recombinant human PTHrP (1-34) anabolic therapy for osteoporosis. *Maturitas* **97**, 53-60, doi:10.1016/j.maturitas.2016.12.003 (2017).

7 Srivastava, M. & Deal, C. Osteoporosis in elderly: prevention and treatment. *Clin Geriatr Med* **18**, 529-555, doi:10.1016/s0749-0690(02)00022-8 (2002).

8 Bilezikian, J. P., Rubin, M. R. & Finkelstein, J. S. Parathyroid hormone as an anabolic therapy for women and men. *J Endocrinol Invest* **28**, 41-49 (2005).

9 Pioszak, A. A., Parker, N. R., Gardella, T. J. & Xu, H. E. Structural basis for parathyroid hormone-related protein binding to the parathyroid hormone receptor and design of conformation-selective peptides. *The Journal of biological chemistry* **284**, 28382-28391, doi:10.1074/jbc.M109.022905 (2009).

10 Dean, T., Vilardaga, J. P., Potts, J. T., Jr. & Gardella, T. J. Altered selectivity of parathyroid hormone (PTH) and PTH-related protein (PTHrP) for distinct conformations of the PTH/PTHrP receptor. *Mol Endocrinol* **22**, 156-166, doi:10.1210/me.2007-0274 (2008).

11 Hattersley, G., Dean, T., Corbin, B. A., Bahar, H. & Gardella, T. J. Binding Selectivity of Abaloparatide for PTH-Type-1-Receptor Conformations and Effects on Downstream Signaling. *Endocrinology* **157**, 141-149, doi:10.1210/en.2015-1726 (2016).

12 Okazaki, M. *et al.* Prolonged signaling at the parathyroid hormone receptor by peptide ligands targeted to a specific receptor conformation. *Proc Natl Acad Sci U S A* **105**, 16525-16530, doi:10.1073/pnas.0808750105 (2008).

13 Ehrenmann, J. *et al.* High-resolution crystal structure of parathyroid hormone 1 receptor in complex with a peptide agonist. *Nat Struct Mol Biol* **25**, 1086-1092, doi:10.1038/s41594-018-0151-4 (2018).

14 Ehrenmann, J., Schoppe, J., Klenk, C. & Pluckthun, A. New views into class B GPCRs from the crystal structure of PTH1R. *Febs Journal* **286**, 4852-4860, doi:10.1111/febs.15115 (2019).

15 Pioszak, A. A. & Xu, H. E. Molecular recognition of parathyroid hormone by its G protein-coupled receptor. *Proc Natl Acad Sci U S A* **105**, 5034-5039, doi:10.1073/pnas.0801027105 (2008).

16 Josephs, T. M. *et al.* Structure and dynamics of the CGRP receptor in apo and peptide-bound forms. *Science* **372**, doi:10.1126/science.abf7258 (2021).

17 Mannstadt, M. *et al.* Efficacy and safety of recombinant human parathyroid hormone (1-84) in hypoparathyroidism (REPLACE): a double-blind, placebo-controlled, randomised, phase 3 study. *Lancet Diabetes Endocrinol* **1**, 275-283, doi:10.1016/S2213-8587(13)70106-2 (2013).

18 Maeda, S. *et al.* Development of an antibody fragment that stabilizes GPCR/G-protein complexes. *Nat Commun* **9**, 3712, doi:10.1038/s41467-018-06002-w (2018).
19 Chan, P. *et al.* Purification of heterotrimeric G protein alpha subunits by GST-Ric-8 association: primary characterization of purified G alpha(olf). *The Journal of biological chemistry* **286**, 2625-2635, doi:10.1074/jbc.M110.178897 (2011).
20 Dixon, A. S. *et al.* NanoLuc Complementation Reporter Optimized for Accurate Measurement of Protein Interactions in Cells. *ACS Chem Biol* **11**, 400-408, doi:10.1021/acschembio.5b00753 (2016).
21 Zhao, L.-H. *et al.* Structure and dynamics of the active human parathyroid hormone receptor-1. *Science* **364**, 148-153, doi:10.1126/science.aav7942 (2019).
22 Ma, S. *et al.* Molecular Basis for Hormone Recognition and Activation of Corticotropin-Releasing Factor Receptors. *Mol Cell* **77**, 669-680 e664, doi:10.1016/j.molcel.2020.01.013 (2020).
23 Zivanov, J., Nakane, T. & Scheres, S. H. W. Estimation of high-order aberrations and anisotropic magnification from cryo-EM data sets in RELION-3.1. *Iucrj* **7**, 253-267, doi:10.1107/S2052252520000081 (2020).
24 Rohou, A. & Grigorieff, N. CTFFIND4: Fast and accurate defocus estimation from electron micrographs. *J Struct Biol* **192**, 216-221, doi:10.1016/j.jsb.2015.08.008 (2015).
25 Punjani, A., Rubinstein, J. L., Fleet, D. J. & Brubaker, M. A. cryoSPARC: algorithms for rapid unsupervised cryo-EM structure determination. *Nat Methods* **14**, 290-296, doi:10.1038/nmeth.4169 (2017).
26 Sanchez-Garcia, R. *et al.* DeepEMhancer: a deep learning solution for cryo-EM volume post-processing. *Commun Biol* **4**, 874, doi:10.1038/s42003-021-02399-1 (2021).
27 Pettersen, E. F. *et al.* UCSF Chimera--a visualization system for exploratory research and analysis. *J Comput Chem* **25**, 1605-1612, doi:10.1002/jcc.20084 (2004).
28 Emsley, P. & Cowtan, K. Coot: model-building tools for molecular graphics. *Acta Crystallogr D Biol Crystallogr* **60**, 2126-2132, doi:10.1107/S0907444904019158 (2004).
29 Adams, P. D. *et al.* PHENIX: a comprehensive Python-based system for macromolecular structure solution. *Acta Crystallogr D Biol Crystallogr* **66**, 213-221, doi:10.1107/S0907444909052925 (2010).
30 Chen, V. B. *et al.* MolProbity: all-atom structure validation for macromolecular crystallography. *Acta Crystallogr D* **66**, 12-21, doi:10.1107/S0907444909042073 (2010).
31 Jumper, J. *et al.* Highly accurate protein structure prediction with AlphaFold. *Nature* **596**, 583-589, doi:10.1038/s41586-021-03819-2 (2021).
32 Jo, S. *et al.* CHARMM-GUI 10 years for biomolecular modeling and simulation. *Journal of computational chemistry* **38**, 1114-1124, doi:10.1002/jcc.24660 (2017).
33 Lee, J. *et al.* CHARMM-GUI supports the Amber force fields. *The Journal of chemical physics* **153**, 35103, doi:10.1063/5.0012280 (2020).
34 Tian, C. *et al.* ff19SB: Amino-Acid-Specific Protein Backbone Parameters Trained against Quantum Mechanics Energy Surfaces in Solution. *J Chem Theory Comput* **16**, 528-552, doi:10.1021/acs.jctc.9b00591 (2020).
35 Lee, J. *et al.* CHARMM-GUI supports the Amber force fields. *J Chem Phys* **153**, 035103, doi:10.1063/5.0012280 (2020).
36 He, X., Man, V. H., Yang, W., Lee, T. S. & Wang, J. A fast and high-quality charge model

for the next generation general AMBER force field. *J Chem Phys* **153**, 114502, doi:10.1063/5.0019056 (2020).

37 Roe, D. R. & Cheatham III, T. E. PTRAJ and CPPTRAJ: software for processing and analysis of molecular dynamics trajectory data. *Journal of chemical theory and computation* **9**, 3084-3095 (2013).

38 Harrigan, M. P. *et al.* MSMBuilder: Statistical Models for Biomolecular Dynamics. *Biophysical journal* **112**, 10-15 (2017).

ACKNOWLEDGMENTS

The cryo-EM data were collected at Advanced Center for Electron Microscopy at Shanghai Institute of Materia Medica, Chinese Academy of Sciences. We are grateful to W.H. and K.W. for collecting the cryo-EM data. This work was supported by National Natural Science Foundation of China (32071203 to L.H.Z.; 82073904 to M.W.W. and 81973373 to D.H.Y.), the National Key R&D Program of China (2019YFA0904200), the Young Innovator Association of CAS (2018325 to L.H.Z.) and SA-SIBS Scholarship Program to L.H.Z. and D.H.Y.; Ministry of Science and Technology (China) grants (2018YFA0507002 to H.E.X. and 2018YFA0507000 to M.W.W.), the Shanghai Municipal Science and Technology Major Project (2019SHZDZX02 to H.E.X.;18ZR1447800 to L.H.Z and 21JC1401600 to D.H.Y.), the CAS Strategic Priority Research Program (XDB08020303 to H.E.X.).

AUTHOR CONTRIBUTIONS

L.H.Z. designed the expression constructs, purified the complexes, prepared the final samples for negative stain and data collection toward the structures, participated in model building and performed structure and function data analysis, prepared figures and wrote the manuscript; L.H.Z. prepared the cryo-EM grids and Q.N.Y. collected cryo-EM images and performed map calculations, built and refined the structure models; Y.W.X. participated in model refinement; X.H.H conducted MD simulations; A.T.D., C.W.C., C.Z. and Y.Z. performed signaling experiments under the supervision of D.H.Y. and M.W.W.; L.H.Z. and H.E.X. conceived the project, wrote the manuscript.

ADDITIONAL INFORMATION

Competing interests: The authors declare that they have no competing interests.

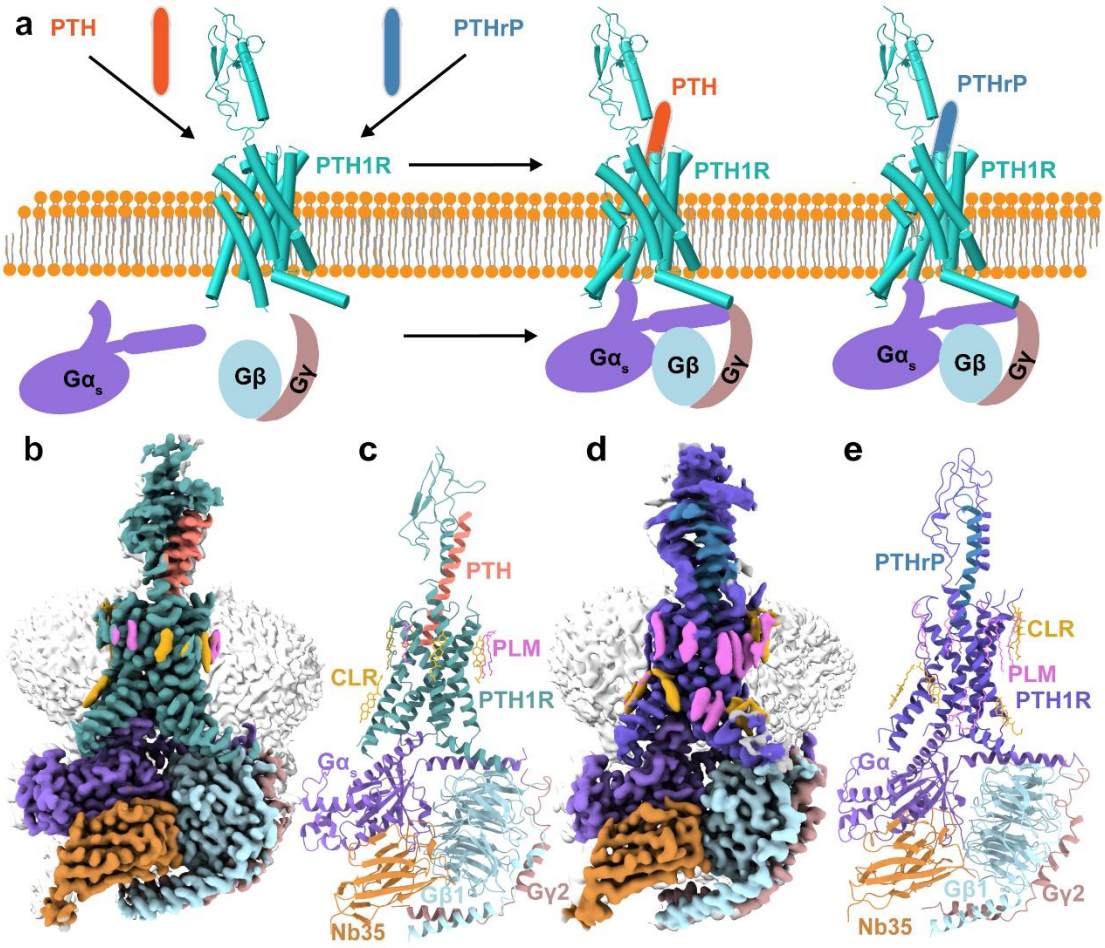

Fig. 1 The overall cryo-EM structures of G_s-coupled PTH1R bound to PTH and PTHrP. (a) Schematic diagram of two endogenous hormones, PTH (salmon) and PTHrP (steel blue) are recognized by PTH1R (light sea green) and exert their effects on bone by activating PTH1R, primarily via G_s-cAMP signaling. G_s is colored in medium purple, Gβ in light blue and Gγ in rosy brown. **(b)** Orthogonal views of the density map and **(c)** model for PTH-PTH1R-G_s complex. The colored cryo-EM density map is shown at the 0.0183 threshold and light gray surface indicates a micelle diameter of 10 nm. Cadet blue, PTH1R; salmon, PTH; medium purple, G_s; light blue, Gβ; rosy brown, Gγ; peru, Nb35; goldenrod, CLR; orchid, PLM. **(d)** Orthogonal views of the density map and **(e)** model for PTHrP-PTH1R-G_s complex. The colored cryo-EM density map is shown at the 0.136 threshold and light gray surface indicates a micelle diameter of 11 nm. Slate blue, PTH1R; steel blue, PTHrP; medium purple, G_s; light blue, Gβ; rosy brown, Gγ; peru, Nb35; goldenrod, CLR; orchid, PLM.

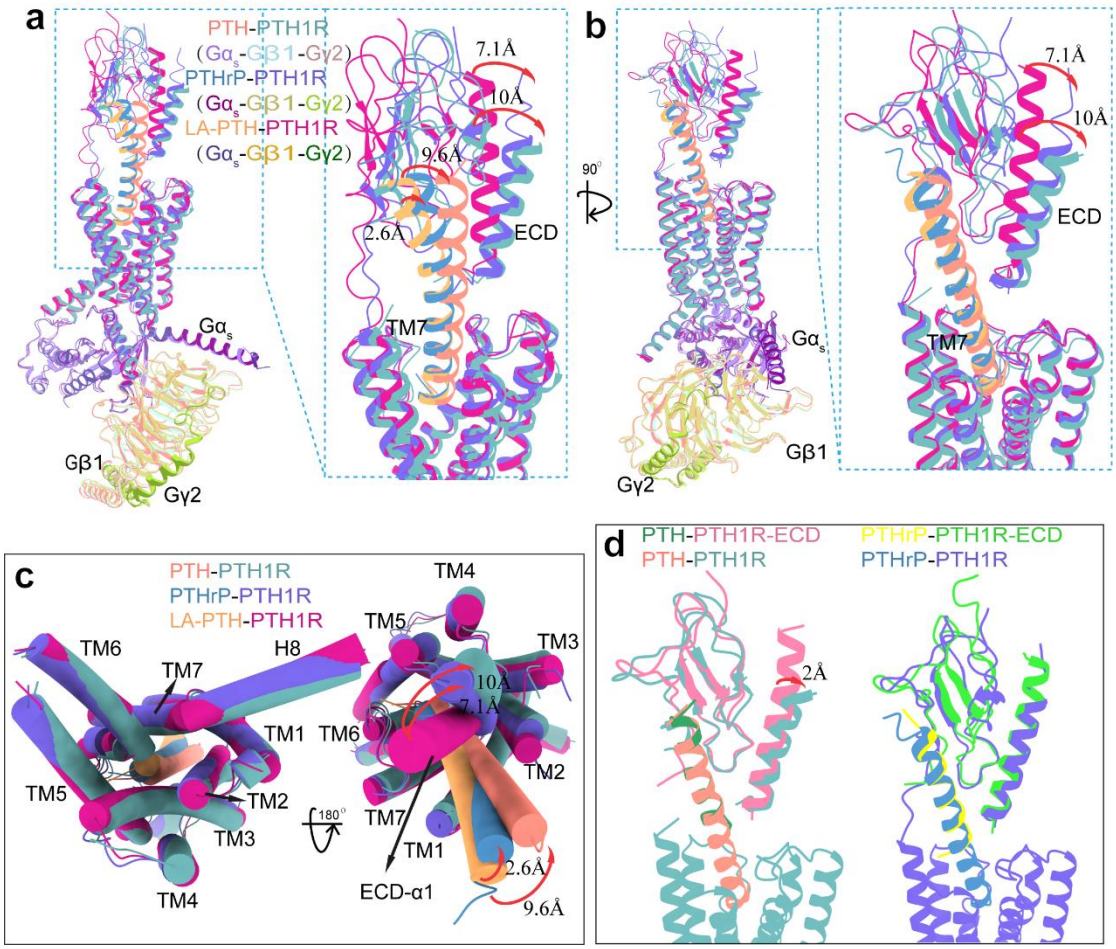

Fig. 2 Structure comparisons of PTH1R-G_s complexes by different ligands. (a-c) Structural comparison of PTH-PTH1R-G_s (salmon, PTH; cadet blue, PTH1R; medium purple, G_s; light blue, Gβ; rosy brown, Gγ), PTHrP-PTH1R-G_s (steel blue, PTHrP; slate blue, PTH1R; purple, G_s; dark khaki, Gβ; yellow green, Gγ) and LA-PTH-PTH1R-G_s (PDB: 6NBF, sandy brown, LA-PTH; medium violet red, PTH1R; dark slate blue, G_s; goldenrod, Gβ; dark green, Gγ) complexes. Notable conformational changes observed in the receptor ECD and the ligand **(a-b)** in the side view and **(c)** cytoplasmic and extracellular view. **(d)** Comparison of the PTH bound ECD in PTH-PTH1R-G_s EM structure with PTH-bound ECD crystal structure (PDB: 3C4M) and PTHrP bound ECD in PTHrP-PTH1R-G_s EM structure with PTHrP-bound ECD crystal structure (PDB: 3H3G), yellow, PTHrP; lime green, ECD; sea green, PTH; pale violet red, ECD.

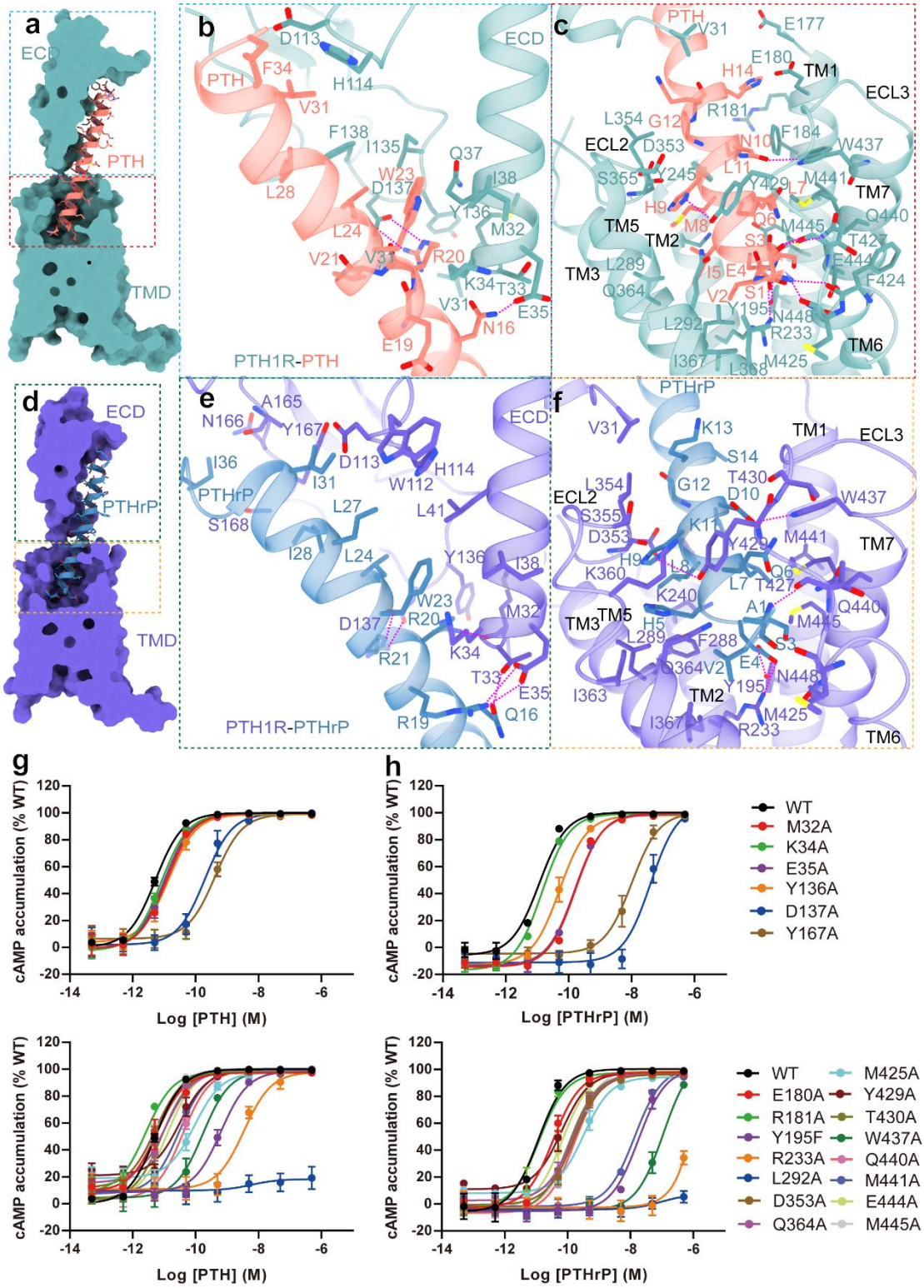

Fig. 3 Molecular recognition of PTH1-34 and PTHrP1-36 by PTH1R. (a) An overall PTH-binding pocket of PTH1R. Cutaway view showing that PTH$^{N\alpha}$ penetrates into a pocket formed by TMD, while its C-terminal half is recognized by the ECD. **(b-c)** Detailed interactions of PTH^{C} with the PTH1R ECD and interactions of PTH$^{N\alpha}$ with the PTH1R TMD pocket, salmon, PTH; cadet blue, PTH1R. The polar contacts are

shown as purple dotted lines. **(d)** An overall PTHrP-binding pocket of PTH1R. Cutaway view showing that $PTHrP^{N\alpha}$ penetrates into a pocket formed by TMD, while its C-terminal half is recognized by the ECD. **(e-f)** Detailed interactions of $PTHrP^{C}$ with the PTH1R ECD and interactions of $PTHrP^{N\alpha}$ with the PTH1R TMD pocket, steel blue, PTHrP; slate blue, PTH1R. The polar contacts are shown as purple dotted lines. **(g-j)** Effect of receptor mutation on PTH and PTHrP-induced cAMP accumulation. **(g-h)** Signaling profiles of PTH1R ECD mutants on PTH and PTHrP-induced cAMP accumulation. **(i-j)** Signaling profiles of PTH1R TMD, ECL2 and ECL3 mutants on PTH and PTHrP-induced cAMP accumulation. cAMP accumulation was measured in wild-type (WT) and single-point mutated PTH1R expressing in HEK293T cells, respectively. cAMP accumulation was normalized to the maximum response of the WT and dose-response curves were analyzed using a three-parameter logistic equation. Data were generated and graphed as means ± S.E.M. of three independent experiments (n = 3) performed in triplicate.

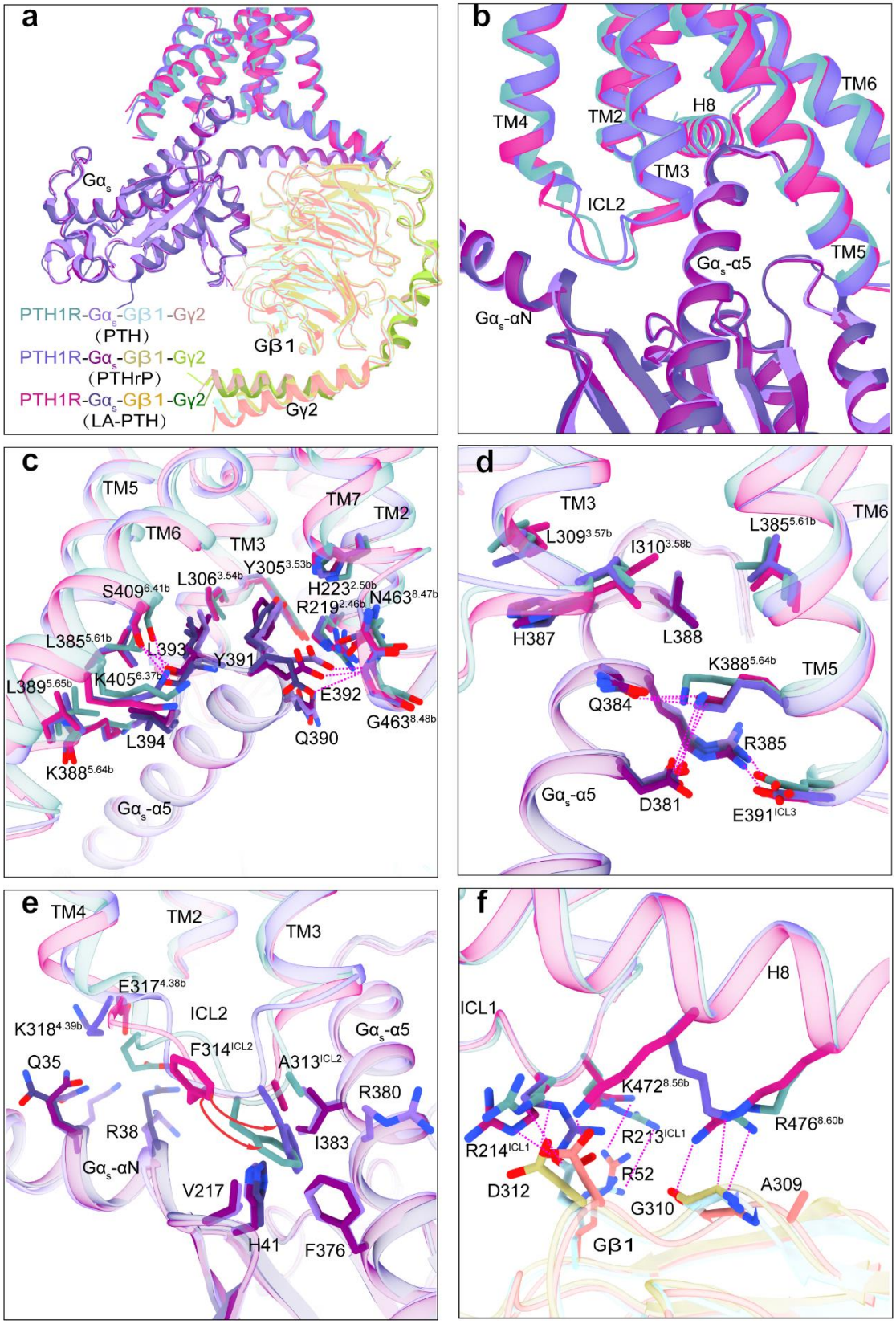

Fig. 4 G protein coupling of multi-agonist-bound PTH1R. (a) Comparison of G protein coupling among PTH, PTHrP and LA-PTH bound PTH1R. The receptors and G proteins are colored as the labels. **(b)** The $G\alpha_s$-α5 helix of the $G\alpha_s$ inserts into an

intracellular cavity of receptor's TMD. **(c-f)** Comparison of the PTH1R-G_s interface, including **(c)** the $G\alpha_s$-α5 C terminus-TMD interface, **(d)** $G\alpha_s$-α5-TM3/TM5 interface, **(e)** ICL2-$G\alpha_s$-αN and $G\alpha_s$-α5 helix interface, **(f)** and helix 8-Gβ1 interface. cadet blue, PTH1R; medium purple, G_s; light blue, Gβ; rosy brown, Gγ in PTH-PTH1R-G_s complex, slate blue, PTH1R; purple, G_s; dark khaki, Gβ; yellow green, Gγ in PTHrP-PTH1R-G_s complex and medium violet red, PTH1R; dark slate blue, G_s; goldenrod, Gβ; dark green, Gγ in LA-PTH-PTH1R-G_s complex The polar contacts are shown as purple dotted lines.

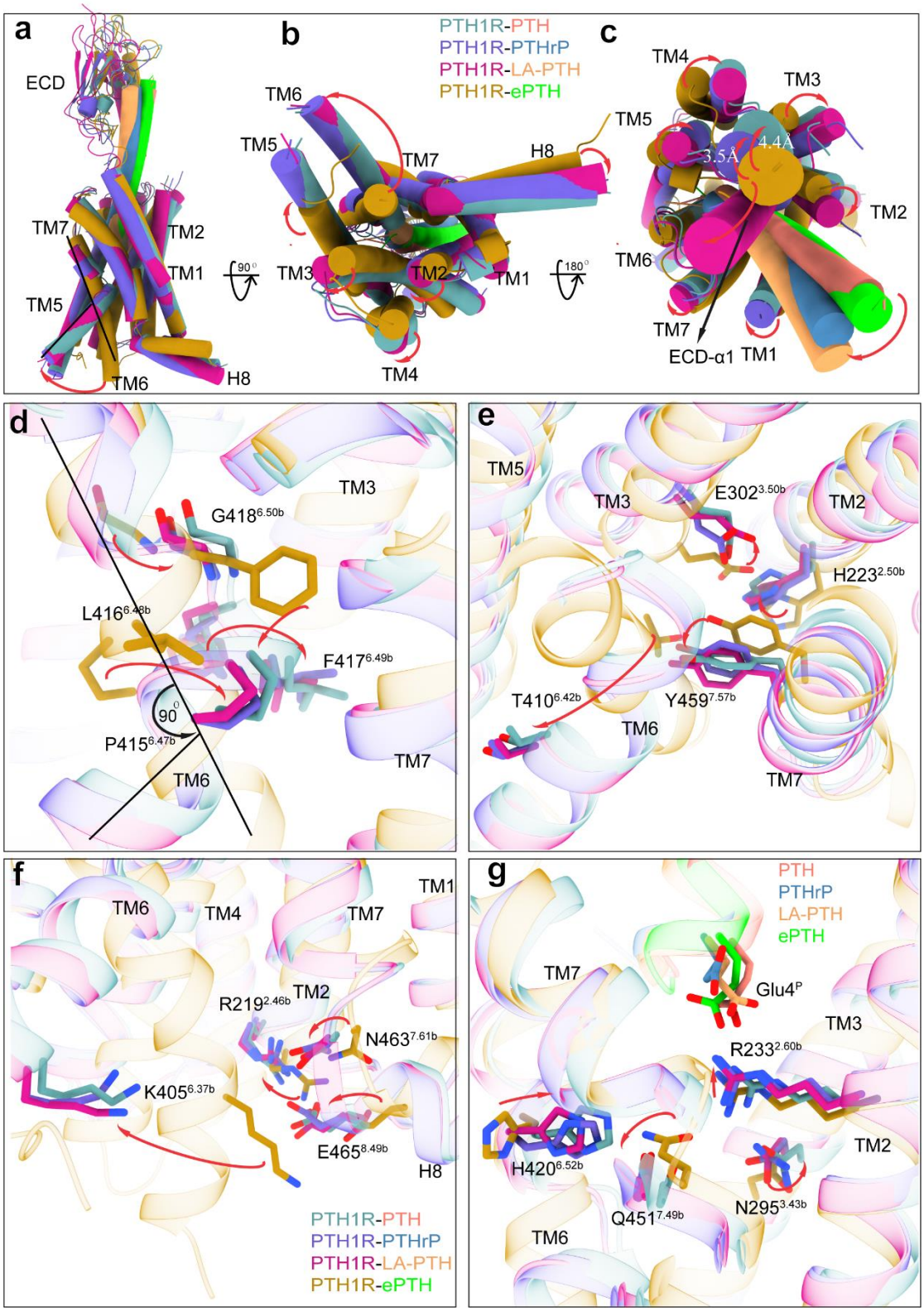

Fig. 5 Structures of the active PTH1R in G protein-bound state and comparison with structure of the active PTH1R in the absence of G protein. (a-c) The structural alignment of ePTH-bound PTH1R (PDB: 6FJ3, lime, ePTH; dark goldenrod, PTH1R) with PTH-bound PTH1R (salmon, PTH; cadet blue, PTH1R), PTHrP-bound PTH1R

716 (steel blue, PTHrP; slate blue, PTH1R) and LA-PTH-bound PTH1R (sandy brown, LA-
717 PTH; medium violet red, PTH1R), which are in G_s bound state, showing different
718 conformational changes of the receptor between PTH1R in G_s bound and no G_s bound
719 states **(a)** in the side view, **(b)** extracellular view and **(c)** intracellular view, the red
720 arrows indicate conformational changes. **(d)** The structural alignment of PTH1R in the
721 absence of G protein and in G protein-bound state, showing the outward bending of the
722 intracellular portion of TM6 of activated PTH1R in G_s-bound state, which results in a
723 kink at the PxxG motif in TM6 and a ~90° angle in the middle of TM6 of the activated
724 PTH1R in G protein-bound state. The TM6 kink in the active PTH1R structure is
725 indicated by a black line. The conserved PxxG motif in TM6 are shown in stick
726 representation. **(e)** Conformational changes during receptor activation in the absence of
727 G protein and in G protein-bound state in HETY network, **(f)** in the II-VI-VII-VIII
728 network, **(g)** and in central polar network. The residues are shown in stick
729 representation and conformational changes are indicated by red arrows.
730